Journal of Materials Chemistry A

ROYAL SOCIETY OF CHEMISTRY

PAPER

View Article Online
View Journal

Cite this: DOI: 10.1039/d5ta07206a

A nanoparticle-decorated bismuth- and nickel-doped $Sr_2Fe_{1.5}Mo_{0.5}O_{6-\delta}$ cathode for enhanced CO_2 reduction in solid oxide electrolysis cells

Mohammadali Emadi and Eric Croiset *

Solid oxide electrolysis cells (SOECs) are a promising technology for CO_2 electrolysis and subsequent conversion to useful chemicals. This paper presents the development of a new cathode material to enhance the performance of SOECs for CO_2 electrolysis. The focus was on the cathode material of the SOEC since it is the limiting factor for CO_2 electrolysis. $Sr_2Fe_{1.5}Mo_{0.5}O_{6-\delta}$ (SFM) has attracted much attention due to its decent performance for CO_2 electrolysis. To enhance the SFM performance, it was modified by doping bismuth and nickel to make a new composition of $Bi_{0.1}Sr_{1.9}Fe_{1.4}Ni_{0.1}Mo_{0.5}O_{6-\delta}$ (BiSFMNi). The Ni-doping made it possible for Fe–Ni nanoparticles to exsolve *in situ* when the material was reduced by 5% H_2/Ar. Structural characterization techniques like XRD showed that, during exsolution, the material changed from a pure double perovskite structure to a mixed-phase material with both Ruddlesden–Popper (RP) and residual double perovskite phases and metallic nanoparticles. Electron microscopy (SEM/TEM/EDS) showed that Ni migrated to the surface of the perovskite bulk where it forms Fe–Ni nanoparticles. This material was then used as the cathode of SOECs, and the results showed that these exsolved Fe–Ni nanoparticles improved the electrocatalytic activity of the CO_2 reduction reaction (CO_2RR). The fabricated cell achieved a current density of 1.3 A cm^{-2} at 800 °C under an applied voltage of 1.6 V, while it was 1.0 A cm^{-2} for the non-exsolved nanoparticle sample.

Received 3rd September 2025
Accepted 4th December 2025

DOI: 10.1039/d5ta07206a

rsc.li/materials-a

1. Introduction

The ever-increasing use of fossil fuels has been the main cause of global warming *via* massive emissions of carbon dioxide (CO_2) in the earth's atmosphere, resulting in atmospheric CO_2 concentration increase from 390 ppm in 2012 to 427 ppm in 2025.[1] This amount of carbon dioxide will have irreparable effects on nature. Among the solutions that were put forward to solve the carbon dioxide emission problem, one solution is carbon capture and utilization. Carbon capture and utilization (CCU) technologies offer a promising avenue to address these dual challenges by not only reducing CO_2 emissions but also converting this greenhouse gas into valuable chemical products. The first step to utilizing CO_2 is its reduction to CO, which can be used further to produce other chemicals when reacted with hydrogen. There are four general methods for converting carbon dioxide into carbon monoxide: thermochemical (thermal energy), electrochemical (electricity), photochemical (photon) and biochemical (biology cultivation) methods. Among these, the electrochemical method has been the focus of much research in recent years. Within electrochemical approaches, solid oxide electrolysis cells (SOECs) have emerged as a particularly promising technology due to their high efficiency due to higher operating temperatures.

Due to the slower rate of CO_2 electrochemical reduction in the SOEC cathode compared to the anode's oxygen evolution process,[2] the system has a high resistance. The performance of many cathode materials is also poor due to their low CO_2 catalytic activity and adsorption capacity. Therefore, the main objective of this research is to enhance the performance of CO_2 reduction in SOECs. It is necessary to develop cathode materials with an optimal combination of high conductivity, structural stability, high CO_2 adsorption capacity, and high electrocatalytic activity for CO_2 splitting.

Nickel, platinum, and other precious metals have been studied for their use as fuel electrode materials, but they face limitations such as thermal instability, corrosion at high temperatures, and/or high cost or scarcity. These issues lead to performance degradation, making pure metals less ideal for long-term SOEC operation.[3] To overcome these challenges, solid oxide cells often use alloys or composite materials that combine the benefits of different metals while minimizing their drawbacks.[4] State-of-the-art electrodes are usually made of cermet, typically Ni with YSZ (Yttria Stabilized Zirconia).[5] However, cermet cathodes such as Ni–YSZ are prone to coke deposition during CO_2 electrolysis.[6,7] As such, there have been efforts to develop alternative cathode materials like perovskites.

Department of Chemical Engineering, University of Waterloo, Waterloo, Ontario, N2L 3G1, Canada. E-mail: smemadif@uwaterloo.ca; ecroiset@uwaterloo.ca

Perovskite materials possess mixed ionic-electronic conductivity and good chemical stability. Among perovskites that have been used in SOECs, $Sr_2Fe_{1.5}Mo_{0.5}O_{6-\delta}$ (SFM) has attracted much attention.[8] SFM has notable conductivity and redox stability, and it is frequently recommended as an electrode for CO_2 electrolysis in SOECs.[8] While SFM is thermally and chemically more robust, especially for CO_2 electrolysis, its catalytic activity, CO_2 adsorption capability, and long-term phase stability still need to be enhanced, especially when compared to the conductivity and catalytic strength of Ni-based cathodes.[9] Researchers have explored a variety of techniques recently to increase its electrocatalytic activity for CO_2 electrolysis, including infiltration technique, doping, and *in situ* exsolution.

Doping SFM with foreign elements to change the defective system and the crystal structure is another method to improve its electrical conductivity and electrocatalytic activity. B-site doping has been well explored in the literature due to successful improvement in cell performance.[10–12] A-site doping, however, has not been thoroughly researched, and a limited number of research papers were found on A-site doping of SFM perovskite for CO_2 electrolysis. A-site doping can influence the crystal structure, oxygen vacancy concentration, and overall stability of the perovskite, thereby impacting its ionic and electronic conductivity. Recent studies have tried to enhance the performance by doping rare-earth and alkaline-earth metals on the A-site. For example, Sun *et al.*[13] investigated the performance of doping La on the $Sr_2Fe_{1.5}Mo_{0.5}O_{6-\delta}$ perovskite. The results showed that $Sr_{1.9}La_{0.1}Fe_{1.5}Mo_{0.5}O_{6-\delta}$ with LSGM as the electrolyte could achieve a current density of 2.76 A cm^{-2} at 850 °C and 1.5 V, which is higher than that of non-doped SFM. This is because La-doping enhances the oxygen surface exchange rate as well as the bulk diffusion coefficient. Yang *et al.*[14] studied the effect of doping bismuth on the A-site of SFM perovskite as the cathode for CO_2 electrolysis. By partially replacing Sr with Bi, the modified SFM showed better CO_2 adsorption and improved oxygen ion conductivity. The cell delivered a high current density of 1620 mA cm^{-2} at 1.6 V and 850 °C.

When a solid solution is formed by mixing two or more components, the atoms of each element are uniformly distributed within the crystal lattice. However, under certain conditions, such as cooling, compositional changes, or changes in temperature and pressure, one of the components may become insoluble, leading to the formation of a separate phase within the structure.[15] The newly formed phase will often have a different composition, crystal structure, and physical properties compared to the original solid solution. This can lead to a range of interesting properties and applications, such as improved mechanical strength, enhanced catalytic activity, and increased conductivity.[15] Exsolution of transition metal particles from the base double perovskite cathode can lead to a promising electrode with enhanced CO_2 catalytic activation.[16,17] Li *et al.*[18] studied the effect of adding Ni–Fe nanoparticles into SFM-SDC uniformly. The chemical adsorption of CO_2 and the kinetics of its surface reactions were both improved by the exsolved NiFe nanoparticles. Under a 1.5 V applied voltage at 800 °C, SOECs using this unique cathode have shown a current density of 2.16 A cm^{-2} and consistent CO_2 electrolysis performance for 500 hours. To effectively accelerate the CO_2RR in SOECs, *in situ* exsolved Fe–Ni nanoparticles on a $Sr_2Fe_{1.35}Mo_{0.45}Ni_{0.2}O_6$ (SFNM) double perovskite substrate (Fe–Ni@SFNM) have been developed by Lv *et al.*[19] The SOEC with the Fe–Ni@SFNM-GDC ($Gd_{0.2}Ce_{0.8}O_{1.9}$) cathode exhibits great stability and no coke deposition for 40 h at 1.2 V, as well as a current density of 0.9 A cm^{-2} at 1.6 V and 800 °C. During the synthesis procedure, nickel was added to the B-site of $Sr_2Fe_{1.5}Mo_{0.5}O_6$ to create a stoichiometric $Sr_2Fe_{1.35}Mo_{0.45}Ni_{0.2}O_6$ (SFNM) double perovskite oxide. Using a high-temperature reduction process, Fe–Ni alloy nanoparticles were exsolved in place and equally anchored on the perovskite surface, while the double perovskite kept its original structure. Lv *et al.*[20] showed that metallic Co can be exsolved from the parent perovskite in a reducing environment, resulting in the creation of cation defects and oxygen vacancies. Metallic Fe may subsequently be exsolved to produce CoFe alloy nanoparticles in $Sr_2Fe_{1.35}Mo_{0.45}Co_{0.2}O_{6-\delta}$ (SFMC), along with the structure changing from double to layered perovskite at 800 °C. At 600 °C, in an oxidizing environment, the spherical CoFe alloy nanoparticles are first converted to flat $CoFeO_x$, then at 800 °C the structure changes back to double perovskite while being entirely dissolved back into the bulk. Due to the synergistic impact of CoFe alloy nanoparticles and plentiful oxygen vacancies at the metal-oxide interfaces, the SFMC cathode decorated with CoFe alloy nanoparticles exhibits 1.2 A cm^{-2} at 1.6 V and 800 °C, which is 50% higher than the parent cathode of SFMC. Zhang *et al.*[21] investigated the stability issued of exsolved nanoparticles on the SFM perovskite. Although the nanoparticles make the material perform better, they are unstable at high voltages (*i.e.*, $\geq$1.6 V). Zhang *et al.* found out that the B-site vacancies are the primary cause of the degradation. Therefore, they supplemented the perovskite with external Fe. The results showed that the supplemented SFNM had better catalytic activity and less degradation. Xi *et al.*[22] explored the exsolution of bimetallic nanoparticles of Fe–Cu on the SFM perovskite. This was done by doping Cu on the SFM structure and then performing reduction treatment. The results showed a current density of 2.5 A cm^{-2} at 1.5 V and 800 °C, which was higher than 1.6 A cm^{-2} of the unreduced electrode. Zhang *et al.*[23] investigated the performance of double perovskite and layered perovskite of SFM with nanoparticles exsolved. By introducing a B-site iron supplement strategy, the authors successfully promote nanoparticle exsolution while preserving the perovskite scaffold, breaking the traditional trade-off. Double perovskite-based nanoparticles (DP-NPs) showed the highest activity, while layered perovskite-based nanoparticles (LP-NPs) offered superior stability. Hu *et al.*[24] proposed a novel strategy of dual-exsolution of nanoparticles on a composite electrode made of SFM and GDC. The cell delivered 1.72 A cm^{-2} at 1.5 V for the CO_2RR, which is almost double that of the SFM/GDC electrode with no nanoparticles. Liu *et al.*[25] studied the effect of doping zinc on Fe-sites of SFM to improve the Fe nanoparticle exsolution and ultimately increase the CO_2RR performance. The cell achieved a high current density of 2.74 A cm^{-2} at 850 °C and 1.6 V, while for SFM with no nanoparticles it was 1.42 A cm^{-2}. Tan *et al.*[26]

presented a high-performance solid oxide electrolysis cell (SOEC) cathode composed of $Pr_{0.4}Sr_{1.6}(NiFe)_{1.5}Mo_{0.5}O_{6-\delta}$ (PSNFM) double perovskite, decorated with exsolved NiFe/FeO_x (NFA@FeO) core–shell nanoparticles. The *in situ* exsolved particles and generated oxygen vacancies significantly enhanced CO_2 adsorption and reduction activity. As a result, the cell achieved a high current density of 1.58 A cm^{-2} at 1.4 V and 800 °C. López-García *et al.*[27] explored a double perovskite, $Sr_xFeCo_{0.2}Ni_{0.2}Mn_{0.1}Mo_{0.5}O_{6-\delta}$ (x = 2.0, 1.9, 1.8), as a cathode material for SOECs. It demonstrates the formation of tunable Fe–Co–Ni ternary alloy nanoparticles *via in situ* exsolution, influenced by reduction temperature and A-site stoichiometry. Exsolution at 600 °C resulted in smaller, more abundant nanoparticles and better CO_2 electrolysis performance than higher-temperature treatments, which led to RP phase formation. The x = 2.0 composition showed superior nanoparticle formation and conductivity. These findings highlight the potential of tailored alloy nanoparticle exsolution for enhancing the SOEC efficiency and broader energy conversion applications.

Exsolution has emerged as a highly promising strategy for enhancing electrode performance in solid oxide electrolysis cells (SOECs). Unlike conventional infiltration methods, exsolved nanoparticles are socketed into the perovskite matrix, offering excellent thermal stability and strong metal–support interaction. This approach not only prevents particle agglomeration under harsh conditions but also introduces abundant active sites and oxygen vacancies, significantly boosting the catalytic activity and long-term durability. Although prior studies have shown that exsolved nanoparticles from perovskite cathodes can improve CO_2 electrolysis performance, most efforts have focused on single-site modifications or base SFM structure. In contrast, our work introduces a dual-site doping strategy, incorporating Bi on the A-site and Ni on the B-site of the SFM double perovskite. This novel approach aims at enhancing catalytic activity through exsolved Ni nanoparticles and also at leveraging Bi doping to improve structural stability and CO_2 adsorption.

2. Experimental methodology

2.1 Perovskite powder synthesis

$Bi_{0.1}Sr_{1.9}Fe_{1.4}Ni_{0.1}Mo_{0.5}O_{6-\delta}$ (BiSFMNi) powder was synthesized using the sol–gel method. Stoichiometric amounts of $Sr(NO_3)_2$, $Bi(NO_3)_3\cdot 5H_2O$, $Fe(NO_3)_3\cdot 9H_2O$, $Ni(NO_3)_2\cdot 6H_2O$ and $(NH_4)_6Mo_7O_{24}\cdot 4H_2O$ (purchased from Fisher Scientific) were dissolved in distilled water under continuous stirring. Then, EDTA–NH_3H_2O combined solution was added, followed by the addition of citric acid. The molar ratio of EDTA : citric acid : total metal ions was kept at 1 : 1.5 : 1. NH_3H_2O was added to adjust the pH value to around 8. The solution was stirred and heated on a hot plate at 80 °C until the gel formed. The gel was then heated on a ceramic dish inside an oven at 400 °C for 4 hours for combustion and removing the organic components and the nitrates. After combustion, the porous material was ground to obtain powder. The powder was sintered at 1100 °C (temperature ramp rate of 3 °C min^{-1}) for 5 hours in air to obtain the final pure phase perovskite powder. $La_{0.4}Ce_{0.6}O_{2-\delta}$ (LDC) powder was prepared with the same procedure for BiSMFNi except that LDC was sintered at 1000 °C. LSGM powder and LSCF/GDC paste were purchased from fuelcellmaterials and used without further modification.

2.2 Cell fabrication

The cells used in this research were electrolyte-supported with the overall structure of BiSFMNi|LDC|LSGM|LSCF-GDC. The LSGM electrolyte powder was uniaxially pressed at 150 MPa using a 30 mm diameter die set to form circular pellets with a thickness of 0.4 mm. The pellet was then heated up to 1450 °C at 2 °C min^{-1} and kept for 10 hours to achieve a fully dense electrolyte. The pellets shrank to a diameter of 24 mm and a thickness of 0.3 mm. The presence of Ni at the electrode–electrolyte interface can lead to undesirable reactions or interdiffusion, potentially reducing the cell performance and stability. To prevent this, a thin LDC buffer layer must be applied between BiSFMNi and LSGM. The LDC layer acts as a chemical barrier, preventing such reactions while maintaining low interfacial resistance due to its high ionic conductivity and compatibility with both LSGM and perovskite-based electrodes. A paste was prepared by mixing the LDC powder with an ink vehicle (fuelcellmaterials) in a 1 : 2 weight ratio of powder to ink. The resulting paste was then spin-coated onto the LSGM substrate and sintered at 1200 °C (temperature ramp of 3 °C min^{-1}) for 5 hours to form a buffer layer prior to deposition of the BiSFMNi cathode. For the air electrode, a commercial LSCF/GDC paste ($La_{0.6}Sr_{0.4}Co_{0.2}Fe_{0.8}O_{3-\delta}$ mixed with GDC) was purchased from fuelcellmaterials. The paste was used as received without further modification and directly applied onto the electrolyte substrate by screen printing. To make the cathode paste for screen printing, the synthesized BiSFMNi powder was mixed with a commercially available ink vehicle (fuelcellmaterials) in a 1 : 1 weight ratio and ball milled to make a paste that was smooth and easy to print. The paste was used to put the cathode layer on top of the LDC layer using a screen printer with an area of 1 cm^2. After screen-printing the electrodes, the cell was sintered at 1100 °C (temperature ramp of 3 °C min^{-1}). The overall cell fabrication process is shown in Fig. 1.

2.3 Testing of the cells

The electrochemical performance of the fabricated SOECs was evaluated using a Fiaxell test station. The cell was first mounted onto the test fixture and sealed with Open Flanges™ inside the furnace. To make sure that the heat was evenly distributed and to avoid thermal shock, the system was heated slowly at 1 °C min^{-1} in air to 800 °C. When the appropriate temperature was reached, argon gas was added to the cathode side to clear out any leftover air from the fuel chamber. Then, the desired reaction gases were supplied to the fuel and air sides, and the system was allowed to stabilize until a steady open-circuit voltage (OCV) was observed. A stable and high OCV, consistent with the theoretical Nernst potential, is not only an indicator of proper electrochemical activity but also confirms good gas tightness of the cell assembly, demonstrating that there is

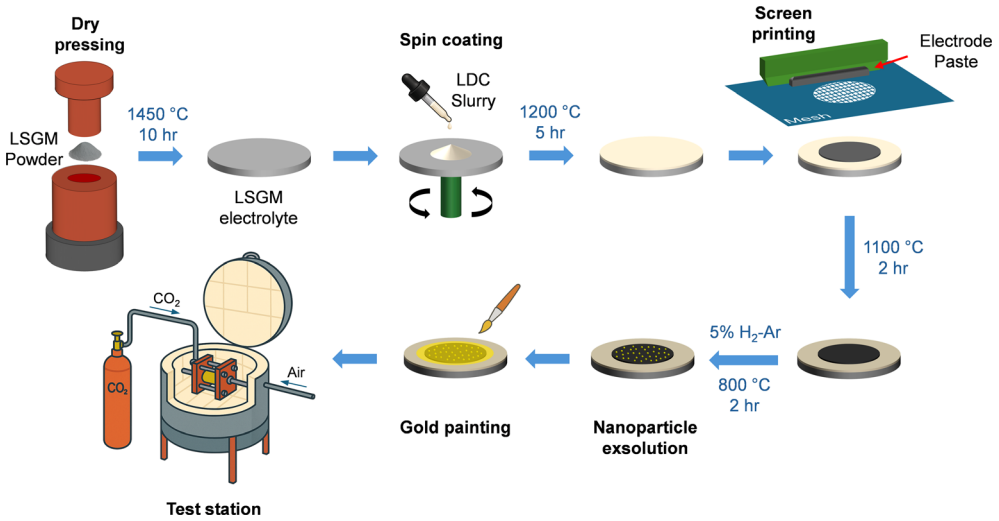

Fig. 1 Overall cell fabrication process.

minimal gas leakage across the electrolyte. After achieving a stable OCV, electrochemical measurements, including *I–V* curve analysis, electrochemical impedance spectroscopy (EIS), and distribution of relaxation times (DRT) analysis, were performed. Following these baseline tests, the fuel side was switched to a 10% H_2–Ar gas mixture for a reduction period to promote *in situ* exsolution of Fe–Ni nanoparticles at the cathode while maintaining air flow on the anode side. After the reduction treatment, the gas supply was switched back to CO_2-containing fuel, and the electrochemical tests were repeated under identical conditions to evaluate the impact of nanoparticle exsolution on CO_2 electrolysis performance. Lastly, the cell temperature dropped in steps to 750 °C and then to 700 °C to see how performance changes with temperature.

2.4 Characterization and electrochemical measurements

Diverse characterization approaches were utilized to examine the structural, morphological, and electrochemical features of the synthesized materials and fabricated cells. Phase identification and crystallographic analysis were conducted *via* X-ray diffraction (XRD) utilizing a Rigaku MiniFlex II diffractometer with Cu Kα radiation. To investigate the chemical states and surface composition of the elements, X-ray photoelectron spectroscopy (XPS) analysis was performed using a Thermo-VG Scientific ESCALAB 250 microprobe. All XPS spectra were calibrated for surface charging by referencing the adventitious carbon (C 1s) peak to 284.8 eV, corresponding to the C–C/C–H bond. To investigate the coke formation, Raman spectrum measurements were carried out on a WITec alpha300 from Oxford Instruments with a 532 nm laser. The surface and cross-sectional microstructures were analyzed utilizing scanning electron microscopy (SEM). A Tescan Vega II SEM was utilized for general imaging and to examine cell architecture and layer thicknesses, whilst high-resolution imaging of electrode surfaces and exsolved nanoparticles was conducted using a Zeiss Merlin SEM. Transmission electron microscopy (TEM) was conducted utilizing a Libra 200 MC TEM for nanoscale structural research, facilitating meticulous examination of particle morphology, interfaces, and crystal lattice fringes. The electrochemical performance was assessed by electrochemical impedance spectroscopy (EIS), and distribution of relaxation times (DRT) analysis, using a Gamry 5000P potentiostat.

3. Results and discussion

The structural configuration of the cell used in this study is shown in Fig. 2. The cell is composed of a dense LSGM electrolyte layer sandwiched between two porous electrodes. The cathode (fuel electrode) is made of a co-doped perovskite material decorated with exsolved metal nanoparticles to enhance CO_2 adsorption and catalytic activity. The anode (oxygen electrode) facilitates the release of oxygen gas and is made of LSCF/GDC.

3.1 Crystal structure and phase characterization

X-ray diffraction (XRD) was used to look at the crystal structure and phase purity of the synthesized perovskite materials. The results, shown in Fig. 3(a), indicate that all the compositions, SFM, Bi-doped SFM (BiSFM), and Bi/Ni co-doped SFM (BiSFMNi), have a pure double perovskite phase with no secondary phases that could be seen. This showed that adding Bi to the A-site and Ni to the B-site was accomplished without changing the structure of the perovskite lattice. Compatibility experiments between BiSFMNi, LDC and LSGM helped to confirm the need of the LDC buffer layer. Binary mixes of BiSFMNi-LDC, BiSFMNi-LSGM, and LDC-LSGM were prepared in a 1 : 1 weight ratio, pressed into pellets, and sintered at 1100 °C for 5 hours. XRD analysis was then performed to evaluate phase stability. As shown in Fig. 3(b), the XRD patterns of BiSFMNi–LDC and LDC–LSGM correspond to the simple superposition of the individual phases, with no evidence of additional diffraction peaks, indicating strong chemical compatibility. A small

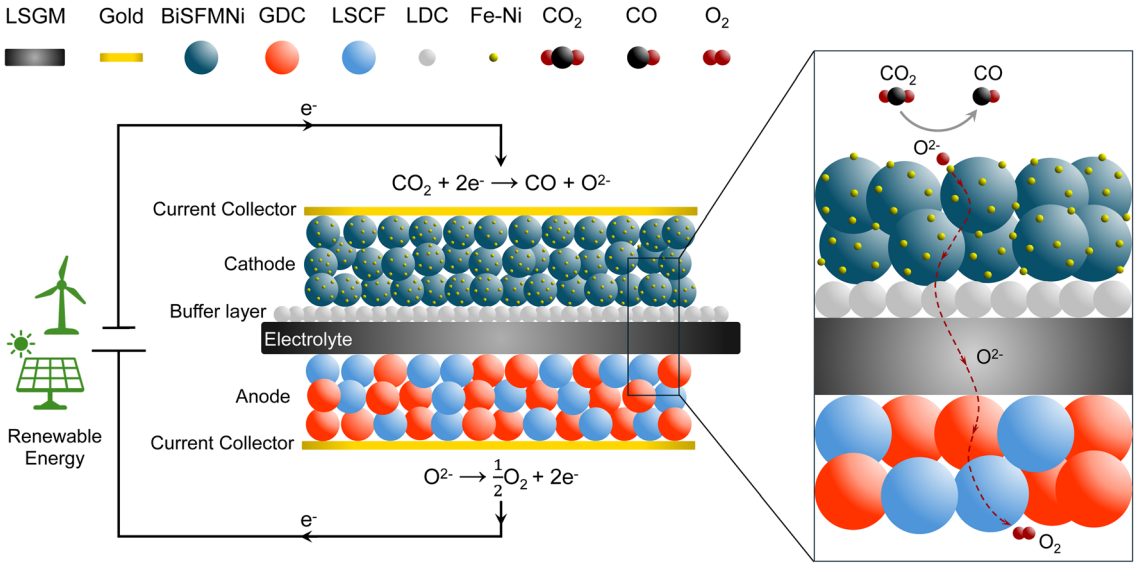

Fig. 2 Schematic of the solid oxide electrolysis cell configuration used in this study.

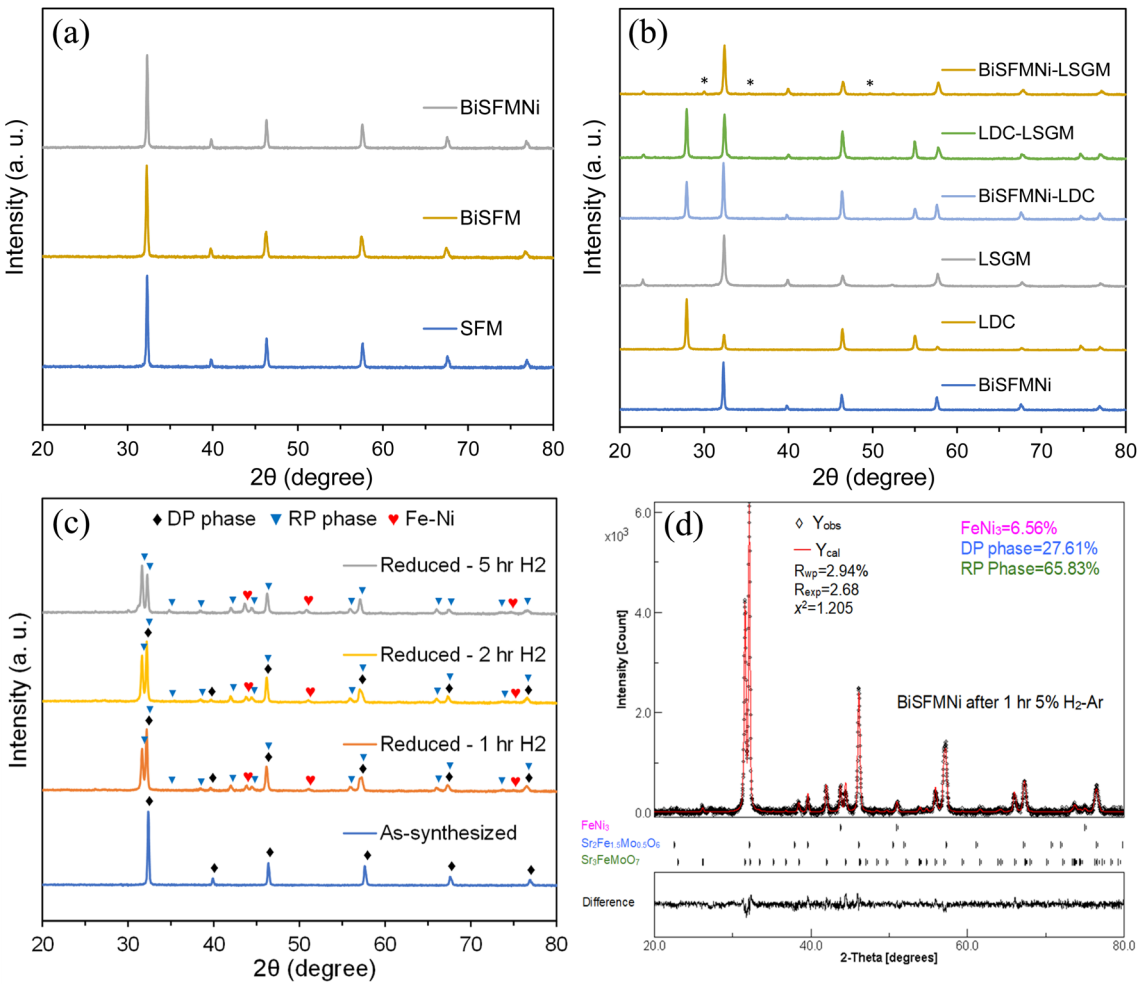

Fig. 3 XRD patterns of (a) SFM, BiSFM, and BiSFMNi powders, (b) chemical compatibility of binary mixes of BiSFMNi-LDC, BiSFMNi-LSGM and LDC-LSGM, (c) XRD patterns of BiSFMNi samples as-synthesized and reduced in 5% H_2/Ar at 800 °C for different durations, and (d) Rietveld refinement that was performed on the XRD pattern of the BiSFMNi sample that had been reduced for one hour.

amount of new phase, at 30° and 35°, in the BiSFMNi–LSGM combination suggests some interfacial interaction between these two materials. These results confirm the need of a thin LDC buffer layer to reduce unwanted interfacial interactions and enhance the chemical stability between the LSGM electrolyte and the BiSFMNi cathode.

XRD analysis was conducted on BiSFMNi samples under reducing conditions to investigate the exsolution behavior; the results are plotted in Fig. 3(c). The oxidized version of BiSFMNi showed a pure double perovskite phase. After 1 hour of reduction in 5% H_2/Ar at 800 °C, however, the XRD pattern showed a mix of leftover double perovskite and newly formed secondary phases of a Ruddlesden–Popper (RP) structure and metallic Fe–Ni. This means that the perovskite scaffold breaks down in part and nanoparticles start to exsolve. The Fe–Ni peaks got stronger as the reduction time increased, while the double perovskite peaks got weaker. This shows that the structure is transforming and that the RP phase is becoming more dominant. After 5 hours of reduction, the XRD pattern predominantly showed the Ruddlesden–Popper phase along with Fe–Ni alloy peaks. This suggests that the original double perovskite structure had largely transformed, and a significant number of nanoparticles had been exsolved. Fig. 3(d) shows the Rietveld refinement that was performed on the XRD pattern of the BiSFMNi sample that had been reduced for one hour. The sample had 6.56% Fe–Ni alloy, 27.61% DP phase, and 65.83% RP phase.

The chemical stability of BiSFMNi was evaluated under CO/CO_2 atmospheres at 800 °C. Powder and pellet samples were exposed for 24 h in either pure CO_2 or 50% CO/CO_2, followed by XRD and Raman analyses. As shown in Fig. S2, BiSFMNi retained its double perovskite structure in both atmospheres, with only weak $SrCO_3$ peaks (~25°) appearing under 50% CO/CO_2 conditions, suggesting minor surface reactions. Raman spectra showed no D (~1340 cm^{-1}) or G (~1580 cm^{-1}) bands, confirming the absence of carbon deposition. These results demonstrate that BiSFMNi possesses excellent phase stability and carbon tolerance in CO/CO_2 environments, supporting its suitability as a durable SOEC cathode material.

3.2 Surface chemical state characterization

X-ray photoelectron spectroscopy (XPS) was performed to investigate the chemical states of Fe, Ni, and O before and after reduction, and the results are shown in Fig. 4. The Fe 2p spectra in Fig. 4(a) show that the sample contained Fe^{3+} and Fe^{2+}. A small Fe^{4+} contribution was also detected in the as-prepared sample, although its intensity was much lower than those of Fe^{3+} and Fe^{2+}. After reduction, a clear Fe^0 peak appeared, showing that some of the iron was reduced. In the same way

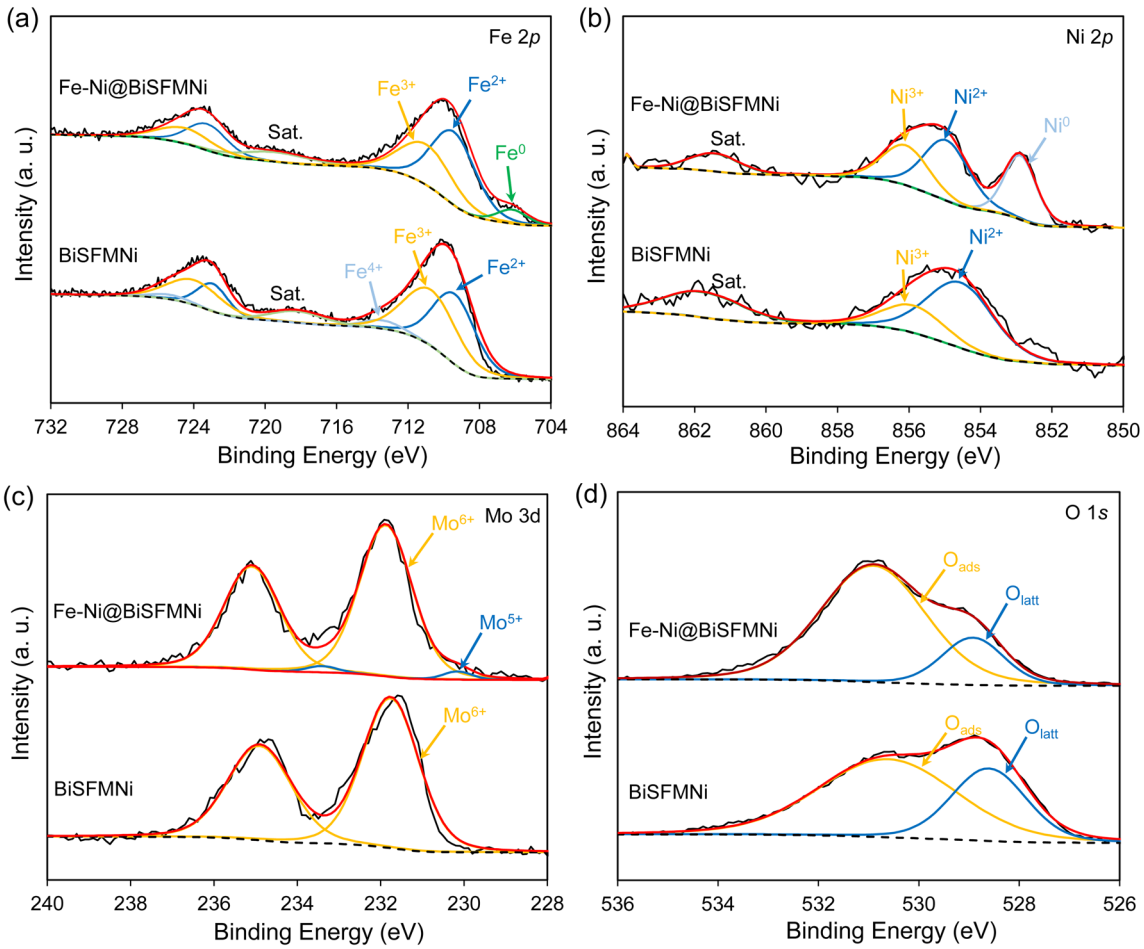

Fig. 4 XPS spectra of (a) Fe 2p, (b) Ni 2p, (c) Mo 3d, and (d) O 1s regions before and after 1 h reduction in 5% H_2–Ar.

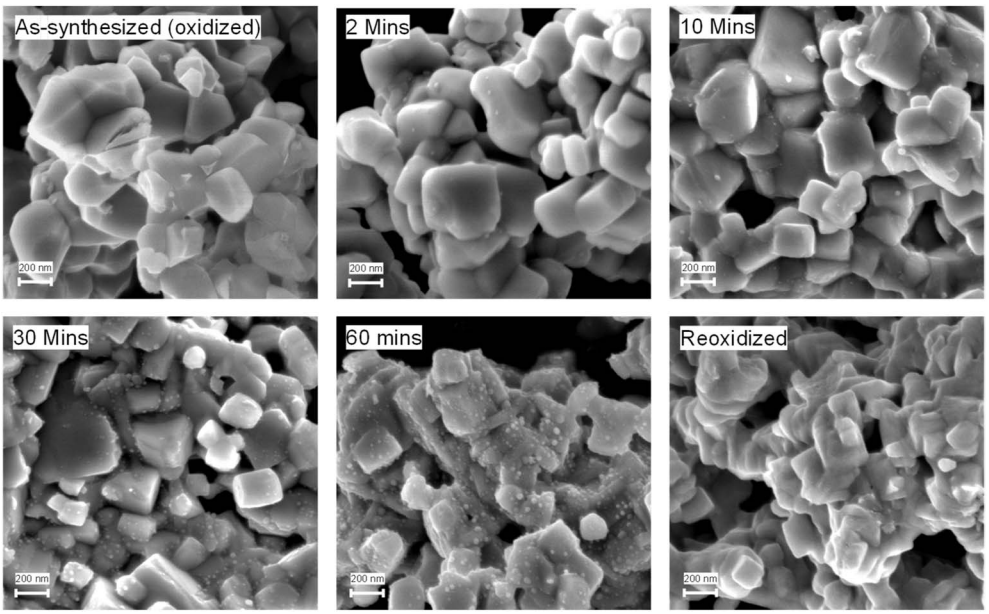

Fig. 5 SEM images of BiSFMNi in three states: as-synthesized, reduced in 5% H_2/Ar at 800 °C for 2, 10, 30 and 60 minutes, and reoxidized in air.

(Fig. 4(b)), the Ni 2p spectra before reduction displayed peaks that matched Ni^{2+} and Ni^{3+}, but following reduction, they changed to produce a Ni^0 signal. From Fig. 4(c), the Mo 3d spectra showed Mo^{6+} in the fresh sample, with the appearance of Mo^{5+} after reduction; however, no Mo^0 peak was observed. This suggests that while Mo underwent partial reduction, it did not participate in the formation of metallic nanoparticles, unlike Fe and Ni. Fig. 4(d) indicates that the O 1s spectra have two peaks: one for lattice oxygen (O_{latt}), which is usually seen at lower binding energies, and the other for adsorbed oxygen species (O_{ads}), which is seen at higher binding energies. After reduction, the O_{latt} peak became less intense, while the O_{ads} peak got stronger. This change indicates that the reduction treatment generates oxygen vacancies in the perovskite lattice. The presence of these vacancies facilitates the migration of B-site cations (Fe and Ni) toward the surface, leading to the *in situ* exsolution of Fe–Ni nanoparticles. These results confirm that Ni and Fe were successfully reduced to their metallic forms, leading to the formation of exsolved Fe–Ni nanoparticles on the perovskite surface.

3.3 Microstructural and morphological characterization

Fig. 5 presents SEM images of BiSFMNi samples at different stages of reduction and reoxidation processes, including the as-synthesized powder, and samples reduced for 2, 10, 30, and 60 minutes, followed by a reoxidized sample. When oxidized, the material had clean, packed grains with smooth surfaces, which is normally expected from a well-sintered perovskite structure with no particles on the surface. As the reduction time increases, a gradual emergence of surface nanoparticles is observed. At 2 and 10 minutes, a few nanoparticles begin to appear, while at 30 and 60 minutes, the number and density of exsolved nanoparticles significantly increase, indicating progressive exsolution of Fe–Ni alloy particles from the perovskite matrix under a reducing atmosphere (5% H_2/Ar at 800 °C). The appearance of surface nanoparticles matches the XRD evidence of the formation of the Fe–Ni phase and a partial change in structure. The grains underneath also look like they are getting rougher on the surface, which could mean that the structure is changing as it moves into the Ruddlesden–Popper phase. In the reoxidized sample, the nanoparticles are no longer visible, and the surface appears smoother and more compact compared to the reduced state. Furthermore, the XRD results of the reoxidized sample (Fig. S1) only show the original double perovskite pattern. The SEM and XRD results indicate that the exsolved Fe–Ni nanoparticles moved back into the perovskite lattice during reoxidation, bringing back the original structure.

The exsolution behavior and structural evolution of BiSFMNi were investigated using transmission electron microscopy techniques. Fig. 6 shows TEM images of the sample before and after reduction at 800 °C for 2 hours in a 5% H_2/Ar atmosphere. More details of TEM analysis are presented in Fig. S4 and S5. In the as-synthesized state, the perovskite exhibits a cubic, dense surface morphology without any apparent nanoparticle decoration. After reduction, clear morphological changes are observed. Numerous nanoparticles emerged and were uniformly distributed on the surface of the perovskite matrix. In the Supplementary Materials, more details of TEM analysis and elemental composition are provided. Additionally, EDS elemental mapping was performed to provide a clearer visualization of the spatial distribution of individual elements across the sample. This technique helped distinguish the regions containing exsolved nanoparticles from the perovskite and Ruddlesden–Popper phases based on elemental composition. The EDS maps, shown in Fig. 6(c), show the spatial distribution of key elements: Fe and Ni signals are strongly localized in the exsolved nanoparticle regions, confirming the formation of Fe–Ni alloy nanoparticles, consistent with Fe–Ni, as identified by

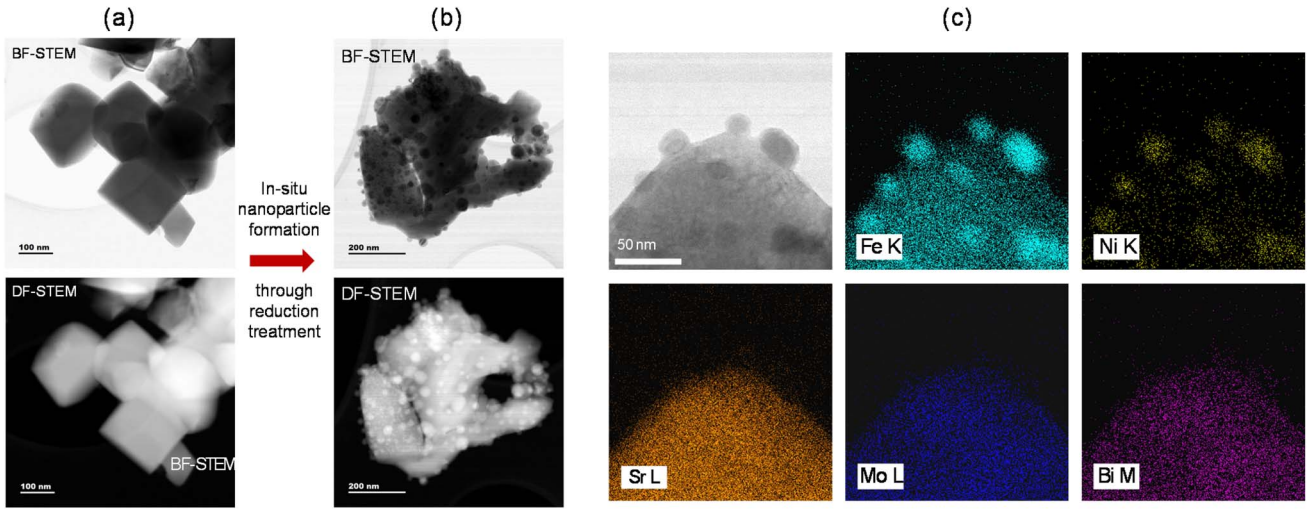

Fig. 6 STEM images of BiSFMNi powder: (a) as-synthesized sample, (b) reduced sample, and (c) STEM image and EDS elemental mapping of BiSFMNi perovskite after reduction treatment showing exsolved nanoparticles.

XRD analysis. In contrast, Sr, Mo, Bi, and O signals are concentrated within the bulk matrix, indicating their retention in the perovskite lattice. The presence of Bi remains uniformly distributed in the matrix, suggesting that Bi remains stable during reduction and does not participate in nanoparticle formation.

Overall, the combination of SEM, TEM, and EDS analyses confirms that the reduction treatment induces selective exsolution of B-site elements (Fe and Ni), while the A-site dopant (Bi) and other structural components remain integrated in the perovskite lattice.

The SEM cross-sectional image of the SOEC in Fig. 7 shows a well-defined multilayer structure, confirming successful layer deposition and good interfacial contact between components. The LSGM electrolyte layer is around 275 μm thick and gives the structural strength and ionic conductivity. On the fuel side (bottom), there is a 40 μm-thick porous cathode (BiSFMNi) that is separated from the electrolyte by a 5 μm LDC buffer layer. This thin layer was deposited *via* spin coating, which proved to be highly effective for achieving a uniform and continuous coating. The LDC layer makes the cathode and the LSGM electrolyte more chemically compatible and stops unwanted reactions at the interface. There is a 55 μm-thick porous anode (LSCF/GDC) on the oxygen side (top). The microstructure of both electrodes is porous, which is necessary for gas diffusion and offering a triple-phase boundary during CO_2 electrolysis. The clear layer boundaries and the strong interfaces show that the screen-printing and sintering procedures worked well. Line EDS analysis across the SOEC cross-section (Fig. S6) confirmed distinct compositional layers with sharp interfaces. The LDC buffer layer was identified from elevated La and Ce signals between the LSGM electrolyte and the BiSFMNi cathode. Strong

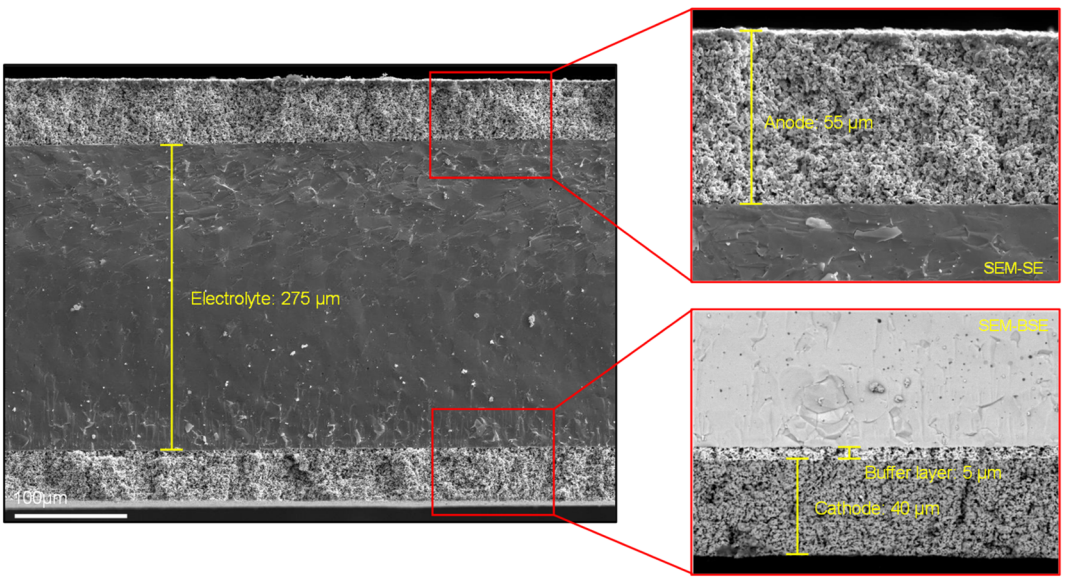

Fig. 7 Cross-sectional SEM image of the fabricated single cell.

Fe, Mo, Bi, and Ni signals verified the BiSFMNi layer, and no significant elemental interdiffusion was observed, confirming the effectiveness of the LDC layer in preventing undesired reactions.

From thermal expansion coefficient (TEC) measurements (shown in Fig. S7), the average CTE values for SFM and BiSFMNi in the temperature range of 25–800 °C are 15.3 × 10^{-6} K^{-1} and 13.9 × 10^{-6} K^{-1}, respectively. The noticeable decrease in TEC after Bi and Ni incorporation indicates that the dopants effectively decrease lattice expansion. This reduction in thermal expansion improves the compatibility of the cathode with typical solid oxide electrolytes. For comparison, LSGM electrolytes exhibit a TEC value of 11.4 × 10^{-6} K^{-1}, while La-doped ceria (LDC), commonly used as an interlayer material, shows a TEC of 13.4 × 10^{-6} K^{-1}. Therefore, BiSFMNi displays a closer thermal match to both LSGM and LDC than pristine SFM, effectively reducing the thermal strain at the cathode–electrolyte interface during high-temperature operation.

3.4 Electrochemical performance

Fig. 8(a) presents the *I–V* curves of cells using BiSFMNi and Fe–Ni@BiSFMNi materials as the cathode for pure CO_2 electrolysis. The BiSFMNi cathode, containing Ni and Bi co-doped perovskite, shows moderate performance with a gradual increase in current density as the voltage increases. In contrast, the Fe–Ni@BiSFMNi sample, in which Fe–Ni alloy nanoparticles were exsolved through a 2 hour reduction process, delivers significantly higher current at higher voltages. At a cell voltage of 1.6 V, the current density for the Fe–Ni@BiSFMNi cathode is 1.3 A cm^{-2}, which is 30% higher than that of 1.0 A cm^{-2} for BiSFMNi. This improvement can be attributed to increased surface catalytic activity. The nanoparticles of Fe–Ni provides numerous reaction sites where CO_2 can absorb and reduce, ultimately increasing the electrochemical reaction rate. This can also be explained by the fact that these nanoparticles increase the

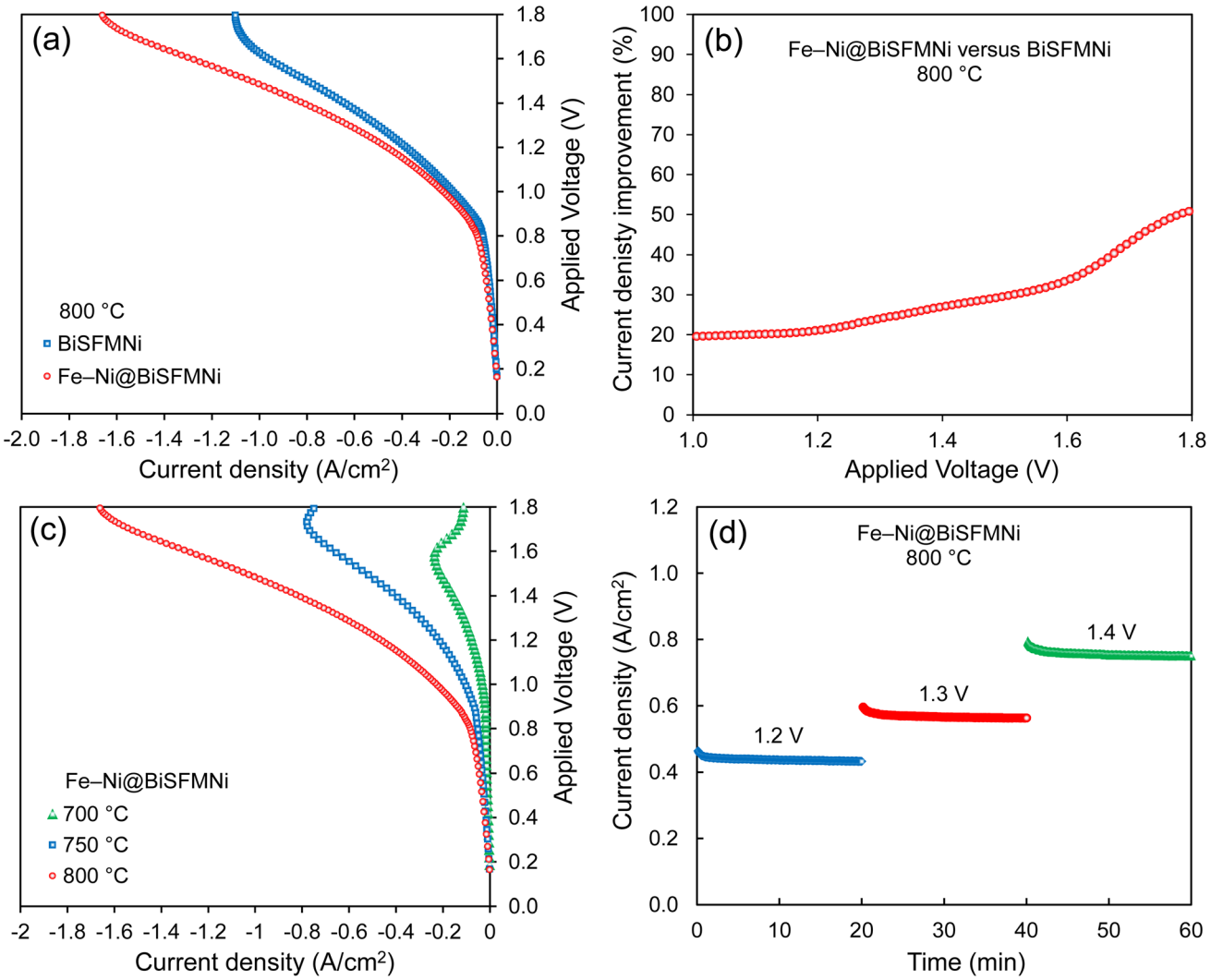

Fig. 8 Electrochemical performance of the cell under CO_2 electrolysis conditions: (a) *I–V* characteristics of BiSFMNi and Fe–Ni@BiSFMNi cathodes, (b) percentage improvement in the current density of Fe–Ni@BiSFMNi over BiSFMNi, (c) *I–V* characteristics of the Fe–Ni@BiSFMNi cathode measured at 700 °C, 750 °C, and 800 °C, and (d) short-term electrochemical stability test under constant voltage operation at 1.0 V, 1.2 V, and 1.4 V.

triple-phase boundary (TPB) density, allowing for more distributed reaction sites.

Fig. 8(b) shows the relative improvement in the current density of Fe–Ni@BiSFMNi *versus* BiSFMNi as a function of applied voltage. This was done to measure how much better the performance was with Fe–Ni nanoparticle exsolution. The data clearly show that increasing the voltage led to an increase in current density. The Fe–Ni@BiSFMNi cathode always outperformed the as-prepared BiSFMNi one over the entire voltage range. At a lower voltage around 1–1.2 V, the improvement in the current density is due to reduction in the activation overpotential. However, this improvement is small as the activation overpotential has a small contribution to the total overpotential. But when the voltage goes above 1.4 V, the improvement gets larger, reaching over 50% at 1.8 V. These results support the idea that exsolution is beneficial to increase the performance of SOEC cathodes, especially when they are under high load or demand.

The Fe–Ni@BiSFMNi-based cell was considered for further analysis. The effect of temperature between 700 and 800 °C on the *I–V* curve was investigated and plotted in Fig. 8(c). As expected, increasing the operating temperature led to increased current densities at all voltages. This improvement can be attributed to faster electrochemical reaction kinetics, especially for the CO_2 reduction process, which is very thermally dependent.[28] At 800 °C, the cell exhibits the highest performance, with a current density exceeding 1.3 A cm^{-2} at 1.6 V. In contrast, at 750 °C and 700 °C, both activation and ohmic losses are more pronounced, leading to a significantly lower current response of 0.67 A cm^{-2} and 0.23 A cm^{-2}, respectively.

Constant-voltage tests were performed at 1.2 V, 1.3 V, and 1.4 V for 20 minutes at 800 °C to see how stable the Fe–Ni@BiSFMNi cathode was in the short term. Fig. 8(d) shows that all three curves start with a drop in current density in the first few seconds. After this change, the current density remains stable, which suggests that the electrode retains its structural and electrochemical integrity throughout the test.

3.4.1 EIS and DRT analysis. Electrochemical impedance spectroscopy (EIS) was used to investigate how the Fe–Ni@BiSFMNi-based cathode behaves under different operating conditions. The EIS measurements show how much resistance arises from different phenomena inside an operating cell. This information is very important for figuring out what steps in CO_2 electrolysis limit performance. Typically, the total resistance

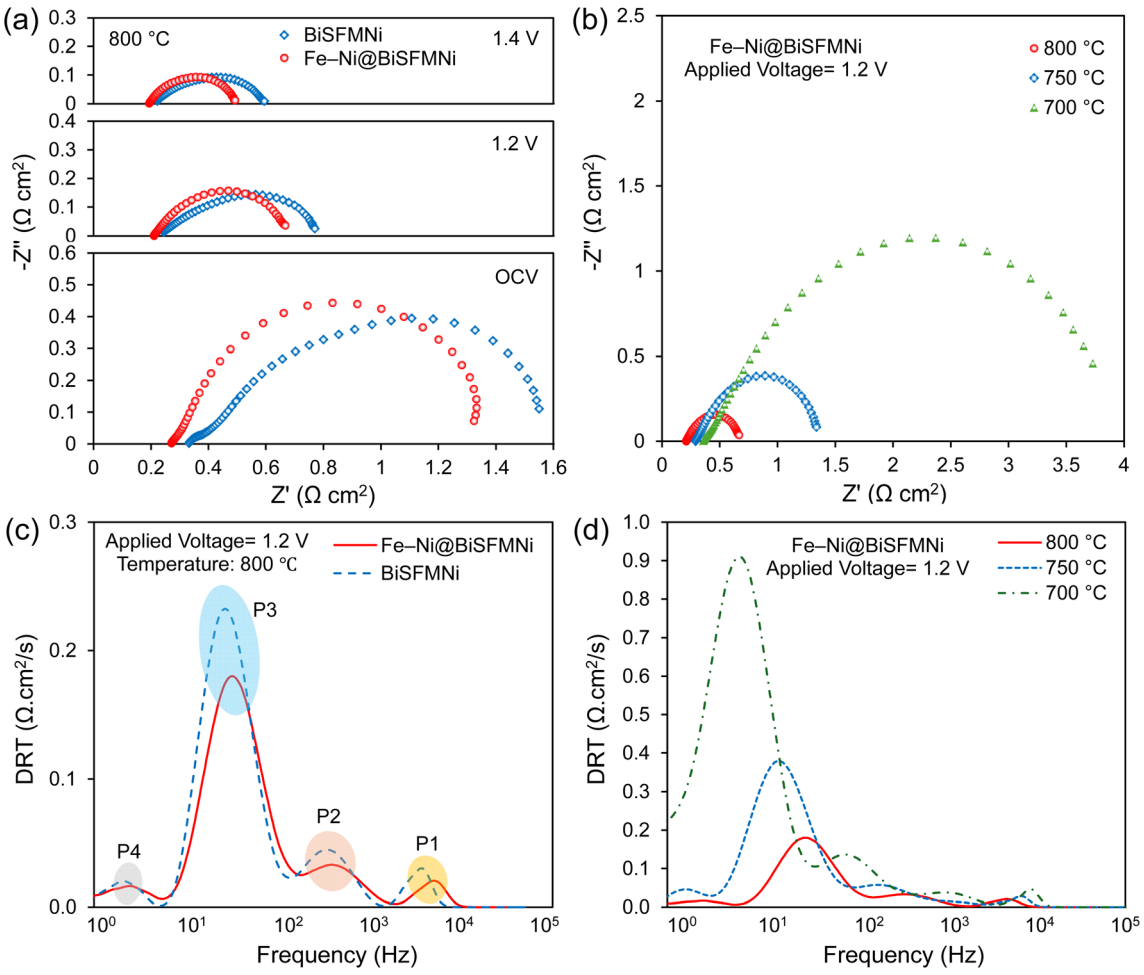

Fig. 9 (a) EIS comparison of Fe–Ni@BiSFMNi and BiSFMNi, (b) temperature dependence of EIS spectra of Fe–Ni@BiSFMNi, (c) DRT comparison of Fe–Ni@BiSFMNi and BiSFMNi cathodes, and (d) DRT spectra of Fe–Ni@BiSFMNi at 800 °C, 750 °C, and 700 °C under 1.2 V applied voltage.

can be separated into two main components: R_s, the ohmic resistance, which includes the ionic resistance of the electrolyte and contact resistance, and R_p, the polarization resistance, which reflects the combined effects of charge-transfer reactions, adsorption, and mass transport limitations at the electrodes.

Fig. 9(a) shows the EIS spectra of the BiSFMNi and Fe–Ni@BiSFMNi cathodes at 800 °C at different voltages (OCV, 1.2 V, and 1.4 V). As the voltage rises, the arc diameter clearly gets smaller (lower R_p) and also shifts a bit to a lower resistance (lower R_s). This pattern shows that charge transfer and catalytic activity are better at higher operating voltages. At 1.4 V, R_s equal 0.2 Ω cm^2 and 0.21 Ω cm^2 for BiSFMNi and Fe–Ni@BiSFMNi, respectively. Fe–Ni@BiSFMNi has smaller arcs (R_p) at all working voltages, which confirms that the exsolved Fe–Ni nanoparticles lower the polarization resistance, from 0.38 Ω cm^2 for BiSFMNi to 0.30 Ω cm^2 at 1.4 V, by increasing the number of reaction sites on the surface and improving the catalytic efficiency. Fig. 9(b) shows how temperature affects the polarization resistance of the Fe–Ni@BiSFMNi cathode at 1.2 V. The size of the arc gets larger resulting in an increase of the R_p from 0.45 Ω cm^2 to 3.6 Ω cm^2 (at 1.2 V) when the temperature decreased from 800 to 700 °C. This shows that higher temperatures favor CO_2 reduction. These EIS results show that nanoparticle exsolution and higher operating temperatures both help reduce polarization losses and make the SOEC work better overall.

Traditional electrochemical impedance spectroscopy (EIS) is useful for measuring the total resistance of a cell, but it doesn't always have enough precision to tell among overlapping electrochemical processes. To get around this problem, the Distribution of Relaxation Times (DRT) analysis is used. DRT breaks down the impedance spectrum into separate time-constant parts, making it easier to find and assign resistive and capacitive processes in the cell. This method is very good at breaking down contributions from electrode polarization, gas diffusion, and charge transfer at the interface.

The DRT deconvolution, Fig. 9(c), shows four separate peaks, which are linked to electrochemical processes that happen at various characteristic frequencies:

- P1 and P2: attributed to oxygen ion transfer in the electrolyte and at interfaces and oxygen evolution at the anode.[19,22,23,29]
- P3: associated with surface processes such as CO_2 adsorption, activation, and electrochemical reduction.[19,22,23]
- P4: gas diffusion process.[19,22,23]

It is observed that P1, P2, and P4 do not change significantly between samples, suggesting that they predominantly reflect bulk ionic transport and gas diffusion phenomena, which are less sensitive to surface modifications. In contrast, P3 shows a more pronounced change, indicating that it is closely related to CO_2 reduction processes at the cathode surface. The smaller P3 peak for Fe–Ni@BiSFMNi demonstrates that the exsolution of Fe–Ni nanoparticles accelerate CO_2 surface kinetics by enhancing adsorption and activation. The exsolution achieved through reduction treatment increases the number of metal-oxide interfaces and oxygen vacancies, both of which facilitate gas-phase reactions and improve electrochemical surface exchange rates. These results are consistent with the *I–V* and EIS studies, which showed improved current density and reduced polarization resistance.

The DRT profiles also show the effect of temperature on the performance, as shown in Fig. 9(d). As the temperature drops, all the peaks move to lower frequencies and are stronger, which means that the kinetics are slower, and the resistive losses are larger. The general pattern is that the polarization resistance increases significantly as the temperature goes down, especially in the low-frequency range where CO_2 reduction happens.

3.4.2 Long-term stability. A long-term electrolysis test was conducted to evaluate the durability of the cell under constant operating conditions. The cell was held at a fixed voltage of 1.3 V, and the current density was monitored continuously for 140 hours. As shown in Fig. 10(a), a sharp initial drop in current density was observed within the first few hours, which can be attributed to the early-stage stabilization of the electrode–electrolyte interfaces and possible restructuring of the electrode surface. Following this initial adjustment, the current density gradually decreased at a rate of approximately 0.6 mA h^{-1}, reflecting slow performance decay over the duration of the test. While longer-term

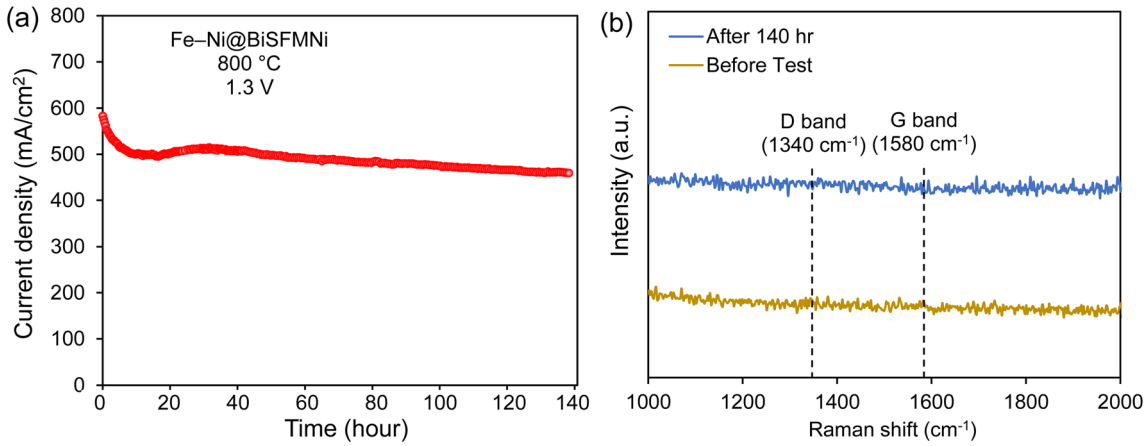

Fig. 10 (a) Long-term CO_2 electrolysis performance at 1.3 V over 140 hours and (b) Raman spectra of the surface of the Fe–Ni@BiSFMNi cathode after the durability test.

testing is needed to evaluate practical SOEC lifetimes, typically exceeding 10 000 hours, the cell maintains relatively high performance over the 140 hour test. The gradual current decay (~0.6 mA h^{-1}) suggests that, if continued linearly, the cathode would not meet practical lifetime requirements. However, the current may stabilize over extended operation due to early-stage electrode restructuring, and further long-term studies are required to confirm stable performance over practical timescales.

Raman spectra collected from the BiSFMNi cathode surface before and after 140 h of CO_2 electrolysis are shown in Fig. 10(b). No characteristic D (1340 cm^{-1}) or G (1580 cm^{-1}) bands associated with carbon species were detected, confirming that no coke formation occurred during long-term operation. The stability of the Raman profile further supports the high tolerance of the BiSFMNi electrode toward carbon deposition and its good catalytic durability during CO_2 electrolysis.

4. Conclusions

$Sr_2Fe_{1.5}Mo_{0.5}O_{6-\delta}$ (SFM), a double perovskite that has been extensively researched, was modified by adding bismuth and nickel to make $Bi_{0.1}Sr_{1.9}Fe_{1.4}Ni_{0.1}Mo_{0.5}O_{6-\delta}$ (BiSFMNi). Under reducing conditions, the phases changed partially and Fe–Ni nanoparticles were exsolved out of the material *in situ*. XRD, Rietveld refinement, and microscopy all showed that there were metallic nanoparticles with a mixed-phase structure. These exsolved nanoparticles added more active sites, made it easier for CO_2 to adsorb to the surface and be activated, as well as speeding up the surface exchange kinetics. The nanoparticle-decorated cathode performed better, reaching a current density of 1.3 A cm^{-2} at 1.6 V and 800 °C, compared to 1.0 A cm^{-2} for the undoped sample. Electrochemical impedance spectroscopy demonstrated lower polarization resistance, from 0.38 Ω cm^2 for BiSFMNi to 0.3 for Fe–Ni@BiSFMNi at 1.4 V, while DRT analysis showed a noticeable drop in low-frequency processes related to surface adsorption and reaction kinetics. These results show how important nanoparticle exsolution is for getting around kinetic barriers and making SOEC cathodes work better.

Author contributions

M. Emadi: conceptualization, investigation, methodology, visualization, writing – original draft. E. Croiset: conceptualization, funding acquisition, supervision, writing – review & editing.

Conflicts of interest

There are no conflicts of interest to declare.

Data availability

Raw data are available from the corresponding author upon reasonable request.

Supplementary information (SI): additional characterization data supporting the main text, including XRD comparisons of as-synthesized, reduced, and reoxidized BiSFMNi; CO/CO_2 stability tests; thermal stability results; and thermal expansion coefficient tests. See DOI: https://doi.org/10.1039/d5ta07206a.

Acknowledgements

This article was supported by the Natural Sciences and Engineering Research Council of Canada, NSERC (grant number RGPIN-07268-2019).

References

1 *Daily CO_2 n.d*, https://co2.earth/daily-co2, accessed March 10, 2025.
2 D. Peterson, E. L. Miller, K. Randolph, P. K.-H. al and W. Dong, Review—Electrochemical CO_2 Reduction for CO Production: Comparison of Low- and High-Temperature Electrolysis Technologies, *J. Electrochem. Soc.*, 2020, **167**, 044508, DOI: 10.1149/1945-7111/AB7099.
3 M. A. Laguna-Bercero, Recent advances in high temperature electrolysis using solid oxide fuel cells: a review, *J. Power Sources*, 2012, **203**, 4–16, DOI: 10.1016/j.jpowsour.2011.12.019.
4 Y. W. Ju, Progress in Materials and Metal Substrates for Solid Oxide Fuel Cells, *Energies*, 2025, **18**, 3379, DOI: 10.3390/EN18133379.
5 M. Shen, F. Ai, H. Ma, H. Xu and Y. Zhang, Progress and prospects of reversible solid oxide fuel cell materials, *IScience*, 2021, **24**, 103464, DOI: 10.1016/J.ISCI.2021.103464.
6 V. Alzate-Restrepo and J. M. Hill, Carbon deposition on Ni/YSZ anodes exposed to CO/H2 feeds, *J. Power Sources*, 2010, **195**, 1344–1351, DOI: 10.1016/J.JPOWSOUR.2009.09.014.
7 E. Tezel, A. Whitten, G. Yarema, R. Denecke, J.-S. McEwen and E. Nikolla, Electrochemical Reduction of CO $_2$ using Solid Oxide Electrolysis Cells: Insights into Catalysis by Nonstoichiometric Mixed Metal Oxides, *ACS Catal.*, 2022, **12**, 11456–11471, DOI: 10.1021/acscatal.2c03398.
8 H. Sun, X. Xu, Y. Song and Z. Shao, Recent Progress in Sr2Fe1.5Mo0.5O6-δ-Based Multifunctional Materials for Energy Conversion and Storage, *Adv. Funct. Mater.*, 2024, **34**, 2411622, DOI: 10.1002/ADFM.202411622.
9 P. Qiu, S. Sun, J. Li and L. Jia, A review on the application of Sr2Fe1.5Mo0.5O6-based oxides in solid oxide electrochemical cells, *Sep. Purif. Technol.*, 2022, **298**, 121581, DOI: 10.1016/j.seppur.2022.121581.
10 Y. Jiang, Y. Yang, C. Xia and H. J. M. Bouwmeester, Sr2Fe1.4Mn0.1Mo0.5O6−δ perovskite cathode for highly efficient CO2 electrolysis, *J. Mater. Chem. A*, 2019, **7**, 22939–22949, DOI: 10.1039/c9ta07689a.
11 C. Xu, S. Zhen, R. Ren, H. Chen, W. Song, Z. Wang, W. Sun and K. Sun, Cu-Doped Sr2Fe1.5Mo0.5O6−δ as a highly active cathode for solid oxide electrolytic cells, *Chem. Commun.*, 2019, **55**, 8009–8012, DOI: 10.1039/c9cc03455b.
12 X. Xi, J. Liu, Y. Fan, L. Wang, J. Li, M. Li, J. Luo and X. Fu, Reducing d-p band coupling to enhance CO2 electrocatalytic activity by Mg-doping in Sr2FeMoO6-δ double perovskite for high performance solid oxide

electrolysis cells, *Nano Energy*, 2021, **82**, 105707, DOI: 10.1016/j.nanoen.2020.105707.

13 C. Sun, L. Bian, J. Qi, W. Yu, S. Li, Y. Hou, L. Wang, J. Peng and S. An, Boosting CO2 directly electrolysis by electron doping in Sr2Fe1.5Mo0.5O6-δ double perovskite cathode, *J. Power Sources*, 2022, **521**, 230984, DOI: 10.1016/j.jpowsour.2022.230984.

14 M. Yang, Z. Yao, S. Liu, J. Wang, A. Sun, H. Xu, G. Yang, R. Ran, W. Zhou, G. Xiao and Z. Shao, Bismuth doped Sr2Fe1.5Mo0.5O6- double perovskite as a robust fuel electrode in ceramic oxide cells for direct CO2 electrolysis, *J. Mater. Sci. Technol.*, 2023, **164**, 160–167, DOI: 10.1016/j.jmst.2023.04.061.

15 G. F. Vander Voort, Metallography and Microstructures, *ASM Handbook*, 2004, vol. 9, DOI: 10.31399/ASM.HB.V09.9781627081771.

16 X. Sun, Y. Ye, M. Zhou, H. Chen, Y. Li, P. Chen, D. Dong, Y. Ling, M. Khan and Y. Chen, Layered-perovskite oxides with *in situ* exsolved Co–Fe alloy nanoparticles as highly efficient electrodes for high-temperature carbon dioxide electrolysis, *J. Mater. Chem. A*, 2022, **10**, 2327–2335, DOI: 10.1039/D1TA07251J.

17 S. Liu, Q. Liu and J. L. Luo, CO2-to-CO conversion on layered perovskite with *in situ* exsolved Co–Fe alloy nanoparticles: an active and stable cathode for solid oxide electrolysis cells, *J. Mater. Chem. A*, 2016, **4**, 17521–17528, DOI: 10.1039/c6ta06365a.

18 Y. Li, B. Hu, C. Xia, W. Q. Xu, J. P. Lemmon and F. Chen, A novel fuel electrode enabling direct CO2 electrolysis with excellent and stable cell performance, *J. Mater. Chem. A*, 2017, **5**, 20833–20842, DOI: 10.1039/c7ta05750d.

19 H. Lv, L. Lin, X. Zhang, D. Gao, Y. Song, Y. Zhou, Q. Liu, G. Wang and X. Bao, *In situ* exsolved FeNi3 nanoparticles on nickel doped Sr2Fe1.5Mo0.5O6−δ perovskite for efficient electrochemical CO2 reduction reaction, *J. Mater. Chem. A*, 2019, **7**, 11967–11975, DOI: 10.1039/C9TA03065D.

20 H. Lv, L. Lin, X. Zhang, Y. Song, H. Matsumoto, C. Zeng, N. Ta, W. Liu, D. Gao, G. Wang and X. Bao, *In Situ* Investigation of Reversible Exsolution/Dissolution of CoFe Alloy Nanoparticles in a Co-Doped Sr2Fe1.5Mo0.5O6−δ Cathode for CO2 Electrolysis, *Adv. Mater.*, 2020, **32**, 1906193, DOI: 10.1002/ADMA.201906193.

21 B. W. Zhang, M. N. Zhu, M. R. Gao, X. Xi, N. Duan, Z. Chen, R. F. Feng, H. Zeng and J. L. Luo, Boosting the stability of perovskites with exsolved nanoparticles by B-site supplement mechanism, *Nat. Commun.*, 2022, **13**, 1–12, DOI: 10.1038/s41467-022-32393-y.

22 X. Xi, Y. Fan, J. Zhang, J. L. Luo and X. Z. Fu, In situ construction of hetero-structured perovskite composites with exsolved Fe and Cu metallic nanoparticles as efficient CO2 reduction electrocatalysts for high performance solid oxide electrolysis cells, *J. Mater. Chem. A*, 2022, **10**, 2509–2518, DOI: 10.1039/d1ta07678g.

23 B. W. Zhang, M. N. Zhu, M. R. Gao, J. Chen, X. Xi, J. Shen, R. F. Feng, N. Semagina, N. Duan, H. Zeng and J. L. Luo, Phase Transition Engineering of Host Perovskite toward Optimal Exsolution-facilitated Catalysts for Carbon Dioxide Electrolysis, *Angew. Chem., Int. Ed.*, 2023, **62**, e202305552, DOI: 10.1002/ANIE.202305552.

24 F. Hu, Y. Ling, S. Fang, L. Sui, H. Xiao, Y. Huang, S. Wang, B. He and L. Zhao, Engineering dual-exsolution on self-assembled cathode to achieve efficient electrocatalytic CO2 reduction, *Appl. Catal., B*, 2023, **337**, 122968, DOI: 10.1016/j.apcatb.2023.122968.

25 S. Liu, M. Yang, R. Xu, X. Xiang, G. Yang, H. Xu, G. Xiao, R. Ran, W. Zhou and Z. Shao, *In situ* passivation of Fe nanoparticles exsolved from perovskite cathodes through zinc doping for CO2 electrolysis, *Green Chem.*, 2023, **25**, 9826–9836, DOI: 10.1039/d3gc03518b.

26 T. Tan, Z. Wang, M. Qin, W. Zhong, J. Hu, C. Yang and M. Liu, *In Situ* Exsolution of Core-Shell Structured NiFe/FeO_x Nanoparticles on $Pr_{0.4}Sr_{1.6}(NiFe)_{1.5}Mo_{0.5}O_{6-\delta}$ for CO_2 Electrolysis, *Adv. Funct. Mater.*, 2022, **32**, 2202878, DOI: 10.1002/adfm.202202878.

27 A. López-García, L. Almar, S. Escolástico, A. B. Hungría, A. J. Carrillo and J. M. Serra, Tuning Ternary Alloyed Nanoparticle Composition and Morphology by Exsolution in Double Perovskite Electrodes for CO_2 Electrolysis, *ACS Appl. Energy Mater.*, 2022, **5**, 13269–13283, DOI: 10.1021/acsaem.2c01829.

28 S. Garg, M. Li, A. Z. Weber, L. Ge, L. Li, V. Rudolph, G. Wang and T. E. Rufford, Advances and challenges in electrochemical CO 2 reduction processes: an engineering and design perspective looking beyond new catalyst materials, *J. Mater. Chem. A*, 2020, **8**, 1511–1544, DOI: 10.1039/c9ta13298h.

29 H. Lv, L. Lin, X. Zhang, R. Li, Y. Song, H. Matsumoto, N. Ta, C. Zeng, Q. Fu, G. Wang and X. Bao, Promoting exsolution of RuFe alloy nanoparticles on Sr2Fe1.4Ru0.1Mo0.5O6−δ *via* repeated redox manipulations for CO_2 electrolysis, *Nat. Commun.*, 2021, **12**, 5665, DOI: 10.1038/s41467-021-26001-8.